

Decarbonizing an industrial process through a combined, high-temperature CSP and sensible heat storage

A. Martín-Alcántara^{a,b,*}, J.J. Serrano-Aguilera^c, A. Sánchez Sánchez de Puerta^a, J.L. Aranda-Hidalgo^{a,d}

^a*Magtel I+D+i, P.E. Las Quemadas, C/ Gabriel Ramos Bejarano, 114, Córdoba, 14014, Spain*

^b*Grupo de Modelización y Sistemas Físicos (FQM-378), Facultad de Ciencias,
Universidad de Córdoba, Campus de Rabanales, Edif. Einstein, Córdoba, 14071, Spain*

^c*Universidad de Málaga, Escuela de Ingenierías Industriales, Campus de Teatinos, s/n, Málaga, 29071, Spain*

^d*Departamento de Mecánica, Escuela Politécnica Superior de Córdoba,
Universidad de Córdoba, Campus de Rabanales, Edif. Leonardo da Vinci, Córdoba, 14071, Spain*

Abstract

Decarbonization is crucial to meet global environmental goals by 2050 and combating climate change. The current work studies a thermal system combining CSP (solar dish) and thermal energy storage (TES) technologies aimed at reducing CO₂ emissions. Given the Direct Normal Irradiance (DNI) profiles of two southern Spain locations (Córdoba and Málaga), numerical simulations have been conducted to analyze the power and the energy provided by this proof of concept on three representative days of 2022 (two solstices and one equinox). One or several solar dishes first increase the temperature of the heat transfer fluid (HTF). Then, following a simple decision-making algorithm, the mass flow enters or bypasses a TES unit. If additional backup energy is required to reach a final temperature, it is supplied externally from e.g. electric sources. A sensitivity analysis has shown that four solar dishes in parallel configuration, combined with a TES unit of aspect ratio $L/D = 1.5$ (if in Córdoba) or $L/D = 1.0$ (if in Málaga), is a suitable solution to effectively reduce the external energy consumed by the system as well as the operation cost and the environmental impact.

Keywords: Decarbonization, numerical simulation, solar dish (CSP), thermal energy storage (TES), high-temperature heat.

1. Introduction

The potential impact of climate change on the global environmental balance and the subsequent

*Corresponding author

Email addresses: antonio.alcantara@magtel.es,
a.martin@uco.es (A. Martín-Alcántara),
jj.serragui@uma.es (J.J. Serrano-Aguilera),
alvaro.sanchez@magtel.es (A. Sánchez Sánchez de

Puerta), joseluis.aranda@magtel.es (J.L. Aranda-Hidalgo)

effects on the global social and economic issues, justify the efforts to achieve a relevant reduction of the CO₂ emissions in the coming years. The most significant advances have been made in electricity generation, mainly due to solar photovoltaic (PV), wind energy, and concentrated solar power (CSP). However, there is still a challenge to overcome in terms of heat supply for the industry, particularly in those considered hard-to-abate sectors [1]. Similarly, renewables still account for a reduced fraction (5.6% in 2021) of global heat generation [2]. According to Madeddu et al. [3] the replacement of fossil fuels for the industry is at the core of the 2050 climate neutrality target of the EU. Direct electrification of heat supply is supposed to be one of the most convenient strategies, but the limits of heat pumps for heat supply at high temperatures restrict the leeway of this scheme for industrial processes that require heat at temperatures higher than approximately 200 °C. It is worth noting that pumps operating above 150 °C can barely be found in the literature [4]. Since this limitation, CSP in combination with thermal energy storage (TES) becomes an ideal complement to reduce CO₂ emissions for such applications, especially in countries such as Spain, due to two key factors. (i) The Spanish generation mix is based on a significant share of non-fossil sources for electricity generation. As of 2022, renewable sources account for 42.2% of the energy in the Spanish grid, along with 20.3% from

nuclear [5]. (ii) Furthermore, the Iberian Peninsula benefits from suitable weather and solar radiation conditions [6] for the massive deployment of CSP, where the case of Andalusia can be highlighted, selecting two of its cities for the location of this study.

In that sense, solar parabolic dishes are commonly accepted as the most efficient CSP technology for the exploitation of solar energy area in the range of kW[7] with a reduced land use. Due to their optical efficiency and the nature of materials (e.g. nickel foam), and of course depending on the dish surface, the temperature increase can be in the order of one thousand degrees. Moreover, the possibility of deploying the dish as close as possible the final application is a huge advantage in reducing thermal and mechanical transport losses. Basically, the dish consists of a parabolic reflector concentrating the radiative energy of the sunlight at the focal point, where the solar receiver is installed. Concentrated radiation enters the receiver through a high-temperature glass window (made of e.g. quartzite). Inside the receiver, different convective-conductive heat exchange processes take place, with the aim of heating a Nickel foam, which is the heart of the solar dish. Two reference works that model the entire performance of the dish are those of Zhu et al. [8] and García Ferrero et al. [9]. Starting from an optical analysis, considering the actual dish geometry through view factors, they formulate the

different thermal processes occurring inside the receiver to eventually provide the outlet temperature. Thermal losses are also considered in both works. The main difference between the two models is the heat transfer considerations between the glass and the foam. In particular, García Ferrero et al. [9] separated on the one hand the heat exchange with the glass and on the other hand the convective heat transfer with the foam. Additional differences have been found in the heat transfer correlations used by each author. This work has been inspired by the aforementioned, but it also considers the heat balance and the source term within the glass window.

To gain flexibility, thermal energy storage has become quite popular in recent years because it represents an ideal solution to decarbonize energy systems, such as power generation on a utility scale, industry, district heating and cooling, buildings and cold chain logistics International Renewable Energy Agency [10]. Depending on the final temperature range, different TES technologies might be used. For instance, in the range 600–700 °C the most suitable strategy is latent or sensible heat storage (e.g. solid-state, molten salts and phase-change materials), which are efficient ($\sim 90\%$) mature technologies with a long lifetime. Thermochemical systems can deal with higher temperature ranges, say 500–900 °C, but their efficiency is lower ($\sim 50\%$) and the level of technological maturity is still limited. Furthermore, the

useful lifetime is considerably shorter [10]. To improve the operation of concentrated solar power plants (CSPs), TES is without a doubt the most suitable solution. Consequently, new and promising TES materials with different configurations are being investigated to minimize costs and to increase operating temperatures in thermal applications [11]. Two main categories can be proposed for TES configurations in CSP plants. If the storage medium is a fluid (e.g. molten salts [12–15] or phase change materials [16–18]) it can be referred to as active storage. Otherwise, if a solid is used to store sensible heat, it is considered passive. Each of these configurations has its own advantages and drawbacks (see [11], but this work is focused on the latter, and more particularly on packed-bed systems, because solids are generally cheaper and they can operate at higher temperatures and heat transfer rates. As an example, Tiddens et al. [19] used porous ceramic bricks as a passive storage system at the Jülich solar tower facility. Typical filler materials for solid TES are sand or concrete Pascual et al. [11], John et al. [20], Villarroel et al. [21], although rocks are also a valid solution [22]. Carbon blocks [23] are becoming a promising alternative [24, 25], and this will be the TES strategy adopted throughout this work.

Therefore, the objective of this paper is to analyze the operation of a thermal system supplying high-temperature heat for the decarboniza-

tion of an industrial activity (e.g. chemical, cement, steel, electrolysis processes, etc.[26–28]) through a simple unsteady mathematical model that integrates CSP (solar dishes) and (carbon blocks) TES technologies. The primary objective is to analyze and to understand the overall performance of the cycle, gaining valuable insight into the configuration and design of CSP & TES devices. Furthermore, the study aims to estimate the timescales involved in the processes, which is important for the practical implementation of the CSP-TES system, ultimately responding to the patent request with application number P202330972[29]. The work is summarized as follows. First, the operation of the system and its elements are summarized. Sect. 3 describes the mathematical models for the solar dish, for the TES, and for the combined CSP-TES solution. Next, the numerical results obtained with the mathematical models are shown and discussed in Sect. 4, analyzing the use of a single or a parallel arrangement of solar dishes, the adopted size of the TES unit, the performance of the entire solution, and its economic and environmental impact. Finally, conclusions are drawn in Sect. 5.

2. Description of the proof of concept

The proposed solution depicted in Fig. 1 integrates solar dish collectors (a parallel arrangement can be used to scale up solar thermal power) (a) and a solid state thermal energy storage system

(TES) (b), governed by a set of valves controlling the system operation. The system is connected to external energy sources (c), preferably those of renewable origin, which may provide additional energy in a external heater (d) to satisfy the constant demand profile ($\dot{Q}_{ref} \simeq 27$ kW at $T_{ref} = 1000$ K) of a given industrial activity (e). It is also acceptable if the heat supply eventually exceeds these reference values. Compressed air at about 5 bar (see e.g. [8, 9] for similar air conditions) is used as heat transfer fluid (HTF). Pressure drops throughout the entire system have not been considered because they will depend on the actual layout of the cycle.

As shown in Fig. 2, air passes through solar dishes and undergoes a temperature increase due to concentrated solar radiation. Subsequently, the heated flowstream enters the TES unit or bypasses it, following a simple decision-making algorithm (see Sect. 3.2) applied at the point O in Fig. 1 to ensure that the reference conditions for the demand (e) are met with the lowest energy, supported by the external backup (d) if required.

The TES unit is a solid-state thermal battery consisting of carbon-porous blocks with high thermal conductivity, intended for heat charge or discharge. The material fillers allow for high temperature (> 2000 °C) storage (see a similar solution in [24, 25]). This thermal storage plays a dual role in the system. On one hand, it facilitates the temperature increase of the mass flow

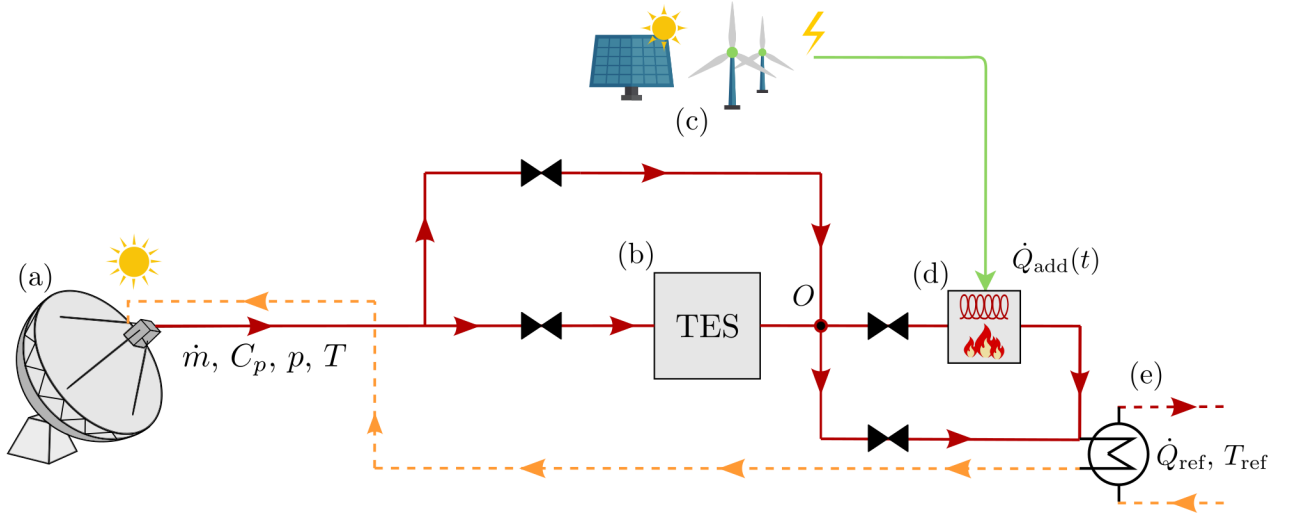


Figure 1: Schematic of the proposed system with external energy hybridization (preferably from renewable origin). The thermal elements considered in this work are labeled as: (a) solar dish, (b) thermal energy storage (TES), (c) external energy sources (preferably of renewable origin) and (d) external heater to meet the demand for industrial activity (e) at $\dot{Q}_{ref} \simeq 27$ kW at $T_{ref} = 1000$.

passing through the unit when the solid temperature is high enough. On the other hand, the heat accumulated in the TES is transferred back to the airflow when the algorithm requires it. It is important to note that while more sophisticated decision-making strategies could be implemented involving either the cost of energy or the amount of CO₂ emissions, this study adopts a simplified logic centered primarily on thermal processes. The evaluation of alternative control methodologies remains a subject for future research.

To carry out a comprehensive analysis, time series from two specific locations in Andalusia (southern Spain), Córdoba and Málaga, which rely on abundant solar resources, have been used. The data includes direct normal irradiance (DNI) and ambient temperature. In addition to the

works of García Ferrero et al. [9] and Zhu et al. [8], Migliari et al. [30] also conducted a similar unsteady analysis. For conciseness, this study only addresses the case in which the TES unit is initially discharged (i.e., it is uniformly set at the waste or return temperature $T_w = 500$ K).

3. Description of the numerical models involved in the cycle

3.1. Solar dish model

The thermal model that predicts the performance of the solar dish integrated in the cycle (see Fig. 2) is described below. It is worth mentioning that while this model shares similarities with the approaches by García Ferrero et al. [9] and Zhu et al. [8], some additional features have been incorporated. The following approach will

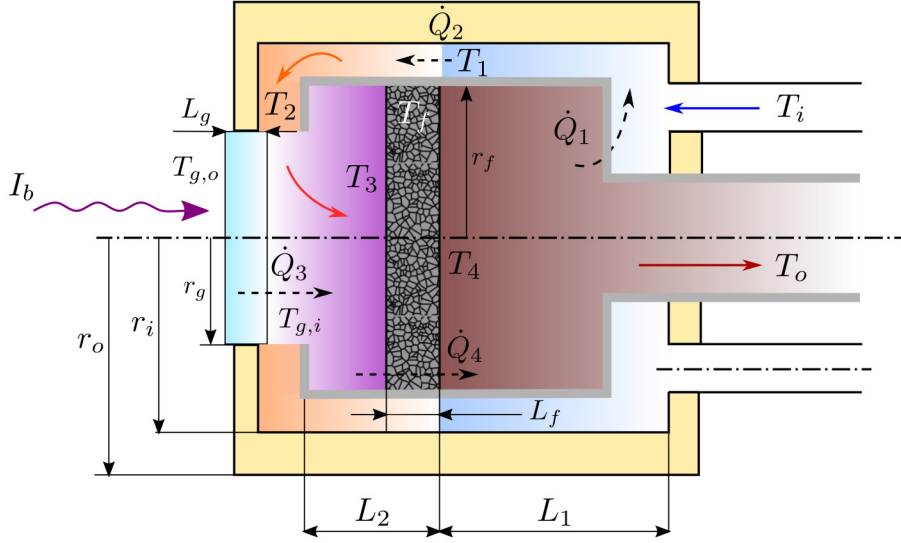


Figure 2: Schematic of the solar dish receiver modeled in this work. The volume is divided into four zones, each representing a different heat transfer process: Zone 1 (blue), Zone 2 (orange), Zone 3 (purple), and Zone 4 (reddish brown). For simplicity, the heat losses are not shown in the figure.

be detailed from the existing zones (1-4) in the receiver.

In Zone 1, the heat transfer fluid (air) enters the receiver at the waste/return temperature delivered by the industrial process T_i . It undergoes a progressive heat exchange with the inner cylinder wall (zone 4 heated by foam) until temperature T_1 is reached. At the same time, the air stream that passes through the foam at temperature T_4 leaves the receiver at the lower temperature T_o . The energy balance relating heat exchange between zones 1 and 4 reads

$$\dot{Q}_1 = \dot{m} C_p(T_{i,1})(T_1 - T_i) = \dot{m} C_p(T_{4,o})(T_4 - T_o), \quad (1)$$

indicating $C_p(T_{a,b})$ the specific heat capacity at constant pressure at the average temperature between a and b . Additionally, Zone 1 can be con-

sidered as a counterflow heat exchanger (see, e.g. Cengel [31]) so that the heat exchange \dot{Q}_1 can be alternatively expressed by using the (natural) logarithmic mean temperature difference (LMTD), i.e.

$$\dot{Q}_1 = U_1 A_1 \frac{(T_o - T_i) - (T_4 - T_1)}{\log \frac{T_o - T_i}{T_4 - T_1}}, \quad (2)$$

where U_1 is the overall (conduction and convection) heat transfer coefficient per unit area of Zone 1, and A_1 the heat exchange area involved in the process. The heat transfer coefficient U_1 has been calculated as in [9] to account for the convection of T_i to T_1 and from T_4 to T_o , and for the conduction through the wall between T_i and T_o .

In Zone 2, the temperature increase from T_1 to T_2 undergone by the mass flow can be expressed as a convection process,

$$\dot{Q}_2 = \dot{m} C_p(T_{1,2})(T_2 - T_1). \quad (3)$$

Similarly to Zone 1, \dot{Q}_2 can also be calculated as the heat transfer in a counter-flow heat exchanger,

$$\dot{Q}_2 = h_w A_2 \frac{(T_w - T_1) - (T_w - T_2)}{\log \frac{T_w - T_1}{T_w - T_2}}, \quad (4)$$

where h_w is the convective heat transfer coefficient at the inner cylinder wall, while A_2 is the surface area. The wall temperature T_w is involved in radiative heat exchange as a gray body. According to the approach by Zhu [8], the thermal equilibrium reads as follows,

$$\dot{Q}_2 = \varepsilon_w F_{fw} [\varepsilon_f A_f \sigma (T_f^4 - T_w^4) + \tau_g \rho_f I_b], \quad (5)$$

with ε_w the emissivity, $A_f = \pi r_f^2$ and T_f the cross-sectional area and the temperature of the foam, F_{fw} the view factor between the foam and the inner cylinder wall, τ_g the glass window transmissivity, ρ_f the reflectivity of the foam, I_b the solar radiation power, and σ the Stephan-Boltzmann constant.

Later, during heat transfer from T_2 to T_3 , the air flow exchanges heat with the inner surface of the glass in Zone 3 [8]. The process can be expressed as the convective heat exchange given by

$$\begin{aligned} \dot{Q}_3 &= \dot{m} C_p (T_{2,3}) (T_3 - T_2) \\ &= A_g h_{g,i} \frac{(T_{g,i} - T_2) - (T_{g,i} - T_3)}{\log \frac{T_{g,i} - T_2}{T_{g,i} - T_3}}. \end{aligned} \quad (6)$$

However, the temperature increase experienced by the glass window due to the incident solar radiation is analyzed separately for the inner and outer surfaces (see Appendix A.3 for further information). For the outer surface of the glass window, heat flow $\dot{q}_{g,o}$ can be defined from the next

balance equation

$$\dot{q}_{g,o} A_g = h_{g,o} A_g (T_a - T_{g,o}) + \varepsilon'_g A_g \sigma (T_a^4 - T_{g,o}^4), \quad (7)$$

and for the inner border, $\dot{q}_{g,i}$ can be obtained from

$$\begin{aligned} \dot{Q}_3 &= \dot{q}_{g,i} A_g + \alpha'_g F_{fg} \varepsilon_f A_f \sigma (T_f^4 - T_{g,i}^4) \\ &\quad + \alpha'_g F_{wg} \varepsilon_w A_w \sigma (T_w^4 - T_{g,i}^4), \end{aligned} \quad (8)$$

with $T_{g,o}$ and $T_{g,i}$, the outer and inner glass temperatures, T_a the ambient temperature, $A_g = \pi r_g^2$ the cross-sectional (effective) area of the glass surface.

The outer border balance in Eq. (7) relates the convective and radiative heat exchanges from the glass window with the surroundings with the diffusive heat flux at the glass outer border $\dot{q}_{g,o}$. In contrast, Eq. (8) relates the inner diffusive flux $\dot{q}_{g,i}$ with the heat transfer to the fluid by convection \dot{Q}_3 , and the radiative exchange with the foam at T_f and the wall at T_w .

In Zone 4, the air has passed through the nickel foam, absorbing the necessary heat to increase the temperature to T_4 . The heat exchange across the foam can be considered convective, i.e.

$$\dot{Q}_4 = \dot{m} C_p (T_{3,4}) (T_4 - T_3) = h_{sf} A_{sf} (T_f - T_{34}), \quad (9)$$

where T_{34} is the average temperature between zones 3 and 4. Since the metal foam is treated as a porous medium, h_{sf} and A_{sf} represent the specific convective heat transfer coefficient and the specific surface area of the structure respectively.

The latter is given by Zhu et al. [8]:

$$A_{sf} = \frac{3\pi d_f}{(0.59 d_p)^2} \left[1 - \exp \left(-\frac{1 - \phi}{0.04} \right) \right], \quad (10)$$

with d_f the thickness of the foam. The ratio between the porous diameter d_p and the foam thickness can be expressed as

$$d_f/d_p = 1.18 \sqrt{\frac{1-\phi}{3\pi}} \frac{1}{1 - \exp[-(1-\phi)/0.04]}. \quad (11)$$

The specific heat transfer coefficient h_{sf} is typically taken from the work of Žukauskas [32], as previously done by e.g. Zhu et al. [8] and Zhao et al. [33].

On the other hand, thermal losses have been computed as in Zhu et al. [8] as follows,

$$\dot{Q}_{g,emission} = \varepsilon'_g A_g \sigma (T_g^4 - T_a^4), \quad (12)$$

$$\dot{Q}_{g,reflectance} = \rho_g I_b, \quad (13)$$

$$\dot{Q}_{f,emission} = \tau'_g F_{fg} \varepsilon_f A_f \sigma (T_f^4 - T_a^4), \quad (14)$$

$$\dot{Q}_{f,reflectance} = \tau'_g F_{fg} \rho_f I_b, \quad (15)$$

$$\dot{Q}_{w,emission} = \tau'_g F_{wg} \varepsilon_w A_w \sigma (T_w^4 - T_a^4), \quad (16)$$

$$\dot{Q}_{convection} = A_g h_{go} (T_g - T_a), \quad (17)$$

which leads to a heat power total loss

$$\begin{aligned} \dot{Q}_{loss} = & \dot{Q}_{g,emission} + \dot{Q}_{g,reflectance} \\ & + \dot{Q}_{f,emission} + \dot{Q}_{f,reflectance} \\ & + \dot{Q}_{w,emission} + \dot{Q}_{convection}. \end{aligned} \quad (18)$$

The overall efficiency of the dish can be expressed as the usual ratio between the energy input and the output, i.e.

$$\eta = 1 - Q_{loss}/I_b, \quad (19)$$

where I_b is the solar radiation power.

The nonlinear algebraic system Eqs. (1) to (9) has been implemented in Python and solved using

the root function with the Levenberg-Marquardt method [34] (see the SciPy optimization toolbox [35]). Unless otherwise specified, the heat transfer coefficients are calculated following the work of García Ferrero et al. [9]. As remarked by them, there is a minimum DNI quantity ensuring the convergence of the system of equations. In the current study, the reference $I_b^0 = 7$ kW has been selected as the threshold value to start the solar dish simulations (notice the mismatch in Fig. 4 comparing I_b with the rest of the magnitudes). Finally, the validation of the solar dish model is shown in Appendix A.

3.2. TES model

The TES unit has been modeled following the work by Schumann [36], which accounts for the one-dimensional convective heat transfer of a fluid at a temperature T that flows through a solid porous medium at a temperature T_s (indistinctly if it is colder or hotter than that of the fluid). Because thermal diffusive effects and external heat sources are considered here, the governing equations become

$$\begin{aligned} \epsilon \left(\frac{\partial T}{\partial t} + u_0 \frac{\partial T}{\partial x} \right) = & \epsilon \alpha \frac{\partial^2 T}{\partial x^2} \\ & - \frac{\lambda_v}{\rho(T) C_p(T)} (T - T_s), \end{aligned} \quad (20)$$

$$\begin{aligned} (1 - \epsilon) \frac{\partial T_s}{\partial t} = & (1 - \epsilon) \alpha_s \frac{\partial^2 T_s}{\partial x^2} \\ & + \frac{\lambda_v}{\rho_s(T) C_{ps}(T)} (T - T_s), \end{aligned} \quad (21)$$

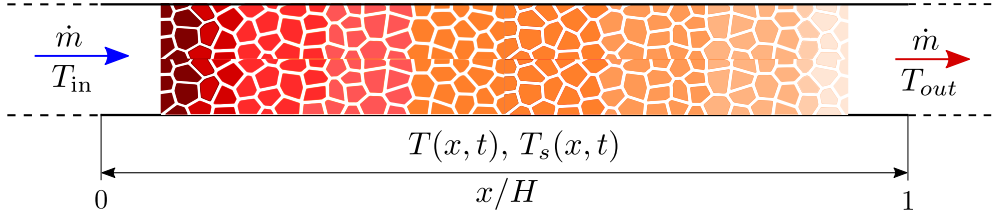


Figure 3: Schematic of the thermal storage system. The porosity of TES in the figure is depicted arbitrarily.

which have to be solved with the appropriate boundary conditions

$$T = T_{in}, \quad \frac{\partial T_s}{\partial x} = 0, \quad \text{at } x = 0, \quad (22)$$

$$\frac{\partial T}{\partial t} = \frac{\partial T_s}{\partial x} = 0, \quad \text{at } x = L, \quad (23)$$

being ϵ the void fraction or porosity, $u_0 = u/\epsilon$ the interstitial velocity, $\alpha = k/(\rho C_p)$ and $\alpha_s = k_s/(\rho_s C_{ps})$ the respective thermal diffusivity for the fluid and for the solid phase, k and k_s the conduction coefficients, C_p and C_{ps} the specific heats at constant pressure, and λ_v the heat transfer coefficient. The initial conditions assume that fluid and solid are in thermal equilibrium, i.e.

$$T = T_s = T_0, \quad \text{at } t = 0. \quad (24)$$

It is convenient to indicate that although some authors [15, 37] introduced additional terms for the improvement of Eqs. (20) and (21) (e.g. the influence of the external wall, thermal losses, or the intra-particle diffusion), it has been shown that the differences are practically negligible compared to those obtained using Schumann's original model[36].

Equations (20) to (24) have been implemented numerically by adopting a finite difference scheme. The diffusive terms are discretized

following a second-order central differencing [38], while the convective term has been upwinded. The temporal discretization follows an implicit Euler method for robustness. The PDE system has been implemented in Python using differentiating matrices to exploit the NumPy[39] capabilities. Exclusively one (temporal) loop exists in the code. Appendix A.3 shows the validation of the TES numerical model.

Finally, for the actual TES used in the proposed thermal solution, the thermophysical properties of the carbon blocks are described in Table 1.

3.3. Combined dish-TES model

Because the waste heat temperature has been considered constant, the temperature of the air exiting a solar dish will depend exclusively on the dish size, the thermophysical properties of the receiver, the mass flow rate (this will be affected by the number of dishes in parallel) and the DNI. Therefore, the solar dish performance remains independent from the rest of the elements of the system. However, the role of the TES may adopt different working strategies switching between charge, discharge, or bypass modes, depending on the following simple decision-making

Table 1: Thermophysical properties of the carbon-block TES material (temperatures in K where needed). Data taken from Butland and Maddison [40].

ρ_G	kg m ⁻³	1800
C_{pG}	J kg ⁻¹ K ⁻¹	4184 (0.54 + 9.11 × 10 ⁻⁶ T - 90.27 T ⁻¹ + 1.593 × 10 ⁷ T ⁻³ - 1.4379 × 10 ⁹ T ⁻⁴)
k_G	W m ⁻¹ K ⁻¹	120

algorithm:

1. $T_{in} \geq T_{ref}$ and $T_{TES}^o \geq T_{ref}$: Charge,
2. $T_{in} \geq T_{ref}$ and $T_{TES}^o < T_{ref}$: Bypass,
3. $T_{in} < T_{ref}$ and $T_{TES}^o \geq T_{ref}$: Bypass,
4. $T_{in} < T_{ref}$ and $T_{in} < T_{TES}^o$ and $T_{TES}^o < T_{ref}$
and $T_{TES}^o < 510$ K: Bypass,
5. $T_{in} < T_{ref}$ and $T_{in} < T_{TES}^o$ and $T_{TES}^o < T_{ref}$
and $T_{TES}^o \geq 510$: Discharge.

In charge mode, high temperature air is used to increase the temperature of the solid fillers within the TES. When the air temperature drops, the process is reversed to energize the airstream performing a heat discharge. Otherwise, the temperature level of the TES is considered to have marginal benefits (or drawbacks), and the bypass mode is activated [although Eqs. (20) to (24) keep evolving in time]. After each of these operation modes, a certain backup power $\dot{Q}_{add}(t)$ is added to the mass flow to reach and maintain the reference conditions required by the industrial process. It should be noted that this is a flexible and extremely simple strategy aimed at reducing the additional energy Q_{add} to meet the thermal demand.

The combination of the thermal elements described in Sect. 3.1 and in Sect. 3.2 has been implemented by directly connecting the outlet temperature of the solar dishes to the corresponding element of the cycle, depending on the aforementioned operating modes. Thus, the TES boundary condition Eq. (22) becomes time dependent, and in consequence it may switch between Dirichlet (in charge or discharge modes),

$$T(t) = T_{in}(t) \equiv T_{os}(t), \quad \frac{\partial T_s}{\partial x} = 0, \quad \text{in } x = 0. \quad (25)$$

and Neumann (or adiabatic) type (when the bypass mode is enabled),

$$\frac{\partial T}{\partial x} = \frac{\partial T_s}{\partial x} = 0, \quad \text{in } x = 0. \quad (26)$$

The outlet boundary conditions remain unchanged from those of the original model [Eq. (22) and Eq. (23)], independently of the operation mode. A quasi-steady approach [note the steady-state formulation in Eqs. (1) to (9)], has been considered for the solar receiver because the time response is fast compared to that of the TES unit.

For illustration's sake, Fig. 4 shows the output temperature of the solar dish of 44 m² used in [8, 9] operating with the same mass flow ratio as that

used by Pacheco et al. [41] ($\dot{m} = 0.043$ kg/s). The return temperature has been fixed to the constant value $T_w = 500$ K, which is similar to that used by [9] (528.66 K/493.88 K in June 22nd/Dec. 22nd), so it will be assumed that the mass flow returns to the dish (or dishes) at that value.

4. Results and discussion

4.1. Solar dish performance for $N = 1, 2$ and 4 dishes in parallel configuration

The solar contribution for $N = 1, 2$ and 4 dishes in parallel (this choice will be justified in Sect. 3.2) is firstly analyzed in Fig. 4 across the days March 22nd (a), June 22nd (b) and December 22nd (c), at the selected locations of southern Spain (Córdoba and Málaga). The number of dishes in parallel (if any) is taken into account in the numerical model through the mass flow rate so that $\dot{m} = \dot{m}_0/N$, with $\dot{m}_0 = 0.043$ kg/s (as previously discussed). The inlet temperature is that of the waste heat, i.e. $T_{in} = T_w$.

When a single dish is used ($N = 1$), the highest outlet temperature reaches about 500 °C, 750 °C and 250 °C on the corresponding day of the study (a)–(c) and (d)–(f). The maximum efficiency [see Eq. (19)] of the solar dish considering the inlet temperature as T_w , is $\eta_{max} \simeq 72\%$, which is found on March 22nd and on June 22nd. However, on December 22nd the radiation impinging the dish decays dramatically, leading to a lower efficiency of 10%, i.e. $\eta \simeq 62\%$. It can be observed that the

influence of location is practically indistinguishable in terms of the DNI (note the temporal evolution of I_b), and only a slightly thinner profile can be identified when comparing (c) vs. (f). In contrast, the ambient temperature presents larger differences due to the coastal climate in Málaga, but with a limited influence on T_o .

For two dishes in parallel configuration ($N = 2$), Fig. 4 shows a significant increase on the outlet temperature, as expected. The maximum temperature at which the airstream exits each of the dishes is now around 750 °C [(a), (d)], 900 °C [(b), (e)] and 500 °C [(c), (f)], i.e. a 50%, a 20% and a 100% compared to the case with $N = 1$. With this configuration, the resulting dish efficiency remains practically unchanged compared to the former case. This is explained by the fact that thermal losses scale up with the increasing temperature for the same ambient temperature, as it can be deduced from Eq. (19).

If the number of dishes in parallel connection is further increased to four ($N = 4$), the efficiency of the dish undergoes a sudden drop at noon on March 22nd and June 22nd. These hours coincide with higher levels of I_b , leading to peak outlet temperatures about 1400 °C [(a), (d)], 1600 °C [(b), (e)] and 600 °C [(c), (f)]. As a result, the thermal losses on March 22nd and June 22nd are high enough to decrease the value of η_{max} , even below the efficiency observed during the early hours of the day.

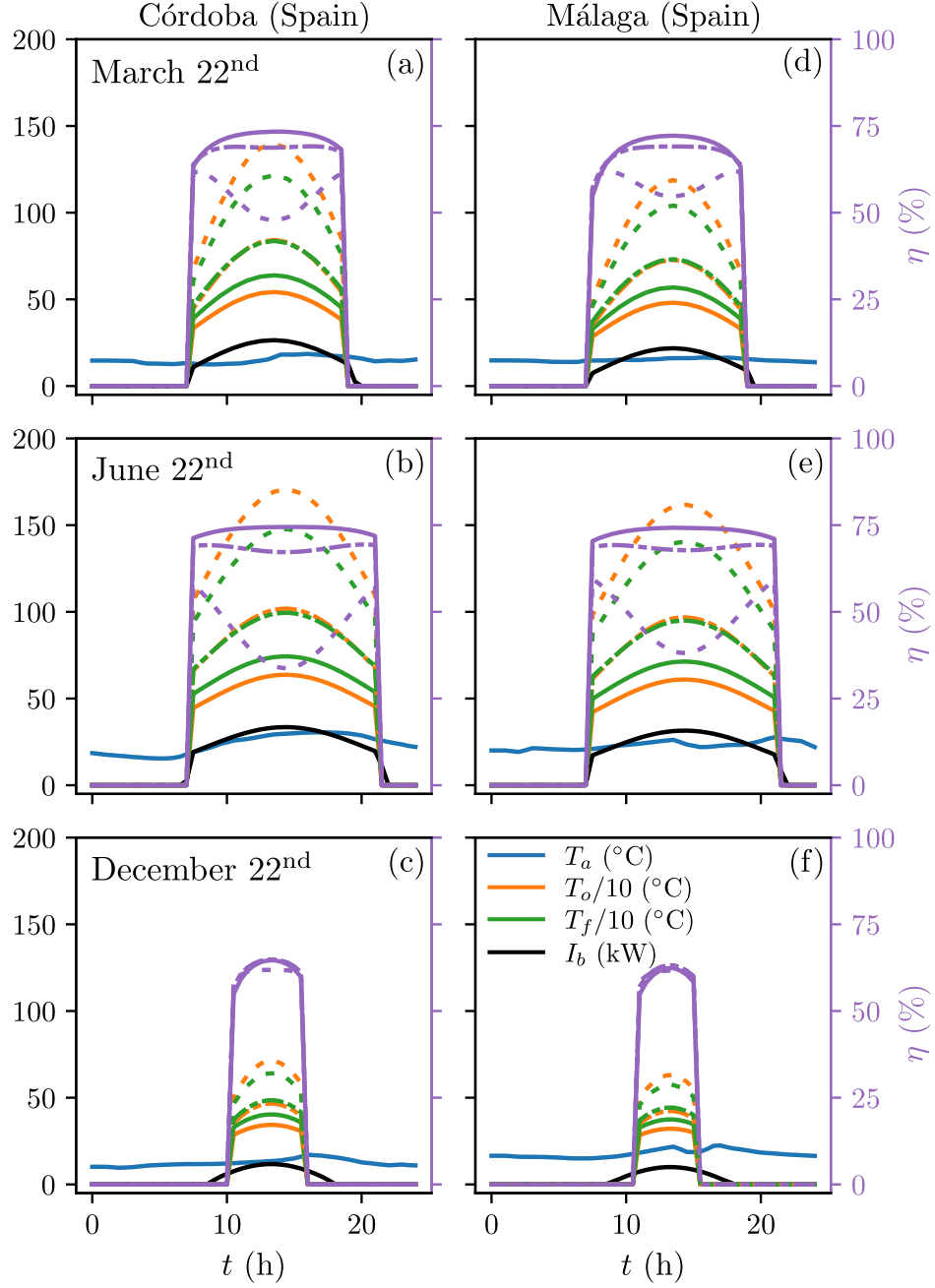


Figure 4: Transient evolution of the (scaled) ambient T_a , output T_o and foam T_f temperatures, solar irradiance I_b , and dish performance η for each of the indicated days in Córdoba (a)–(c) and in Málaga (d)–(f). Solid lines: one solar dish ($N = 1$), dashed: two solar dishes in parallel connection ($N = 2$), dashed-point: four solar dishes in parallel connection ($N = 4$).

4.2. TES sizing procedure

A single TES unit either receives the mass flow exiting the solar dishes at the corresponding outlet temperature (if in charge or discharge modes)

or it only contains and evolves the heat transfer internally (if in bypass mode). Although the aperture area of the solar dish has been fixed at 44 m^2 (as that used by Zhu et al. [8], García Fer-

rero et al. [9]), the appropriate TES size needs to be determined. Dimensional analysis is an effective approach to establish a functional dependence among a reduced set of dimensionless parameters [42, 43]. Because one of the main interests in this work is to determine the most convenient size of the TES to reduce the backup energy Q_{add} necessary to feed the industrial process, the following dependence can be established:

$$Q_{\text{add}} = f(L, D, \dot{m}, \dot{m}_0, \rho_0), \quad (27)$$

where L is the TES length and D is the diameter, \dot{m} is the mass flow rate passing through each of the dishes, $\dot{m}_0 = 0.043 \text{ kg/s}$ is the total mass flow rate considered in this work, and ρ_0 is the air density in standard conditions. With these variables, the basic magnitudes of *length*, *mass* and *time* are covered, and three independent dimensionless groups can be built,

$$\tilde{Q}_{\text{add}} \equiv Q_{\text{add}} \frac{\rho_0 D}{\dot{m}_0^2} = f(L/D, \dot{m}_0/\dot{m} \equiv N), \quad (28)$$

namely the dimensionless energy \tilde{Q}_{add} , the aspect ratio L/D and the number of solar dishes in parallel connection N . However, since \dot{m}_0^2 is very small, it is convenient to express Eq. (28) as

$$\begin{aligned} \tilde{Q}_{\text{add}} \equiv Q_{\text{add}}/Q_0 &\equiv \frac{Q_{\text{add}}}{\dot{m} C_p(\bar{T})(T_{\text{ref}} - T_w) t_{\text{day}}} \\ &= f(L/D, N), \end{aligned} \quad (29)$$

with

$$Q_0 \equiv \dot{m} C_p(\bar{T})(T_{\text{ref}} - T_w) t_{\text{day}} \quad (30)$$

the amount of (theoretical) energy required to elevate the waste temperature T_w to that of reference

T_{ref} demanded by the industrial process ($\dot{Q}_0 \simeq 27 \text{ kW}$ and $Q_0 \simeq 650 \text{ kWh}$).

Figure 5 displays the relationship Eq. (29) in terms of the energy reduction \mathcal{R} with respect to Q_0 ,

$$\mathcal{R} \equiv 1 - \frac{\bar{Q}_{\text{add}}}{Q_0}, \quad (31)$$

where \bar{Q}_{add} stands for the yearly-averaged added energy defined as

$$\bar{Q}_{\text{add}} = \frac{1}{t_y} \int_0^{t_y} Q_{\text{add}}(t) dt, \quad (32)$$

with t_y the total yearly time in the corresponding units. Because the days in the study represent two solstices (22nd June and 22nd December) and one equinox (22nd March), Eq. (32) can be approximated by

$$\bar{Q}_{\text{add}} \simeq \frac{1}{4} \left(2 Q_{\text{add}}^{22^{\text{nd}} \text{ March}} + Q_{\text{add}}^{22^{\text{nd}} \text{ June}} + Q_{\text{add}}^{22^{\text{nd}} \text{ Dec}} \right), \quad (33)$$

assuming that the year 2022 is fully represented by these four dates, and that the fall equinox is similar to that of spring.

The calculation of each term Q_{add}^i (with $i = 22^{\text{nd}} \text{ March}, 22^{\text{nd}} \text{ June}, \text{ or } 22^{\text{nd}} \text{ December}$) in Eq. (33) has been conducted by integrating numerically the system of equations governing the entire cycle operation (see Sect. 3),

$$Q_{\text{add}}^i = \int_0^{24 \text{ h}} \dot{Q}_{\text{add}}^i(t) dt, \quad (34)$$

where $\dot{Q}_{\text{add}}^i(t)$ is the heat power necessary to meet the industrial process demand instantaneously.

The numerical code has been run for the ranges $0.25 \leq L/D \leq 2.00$ (with a resolution of 0.25)

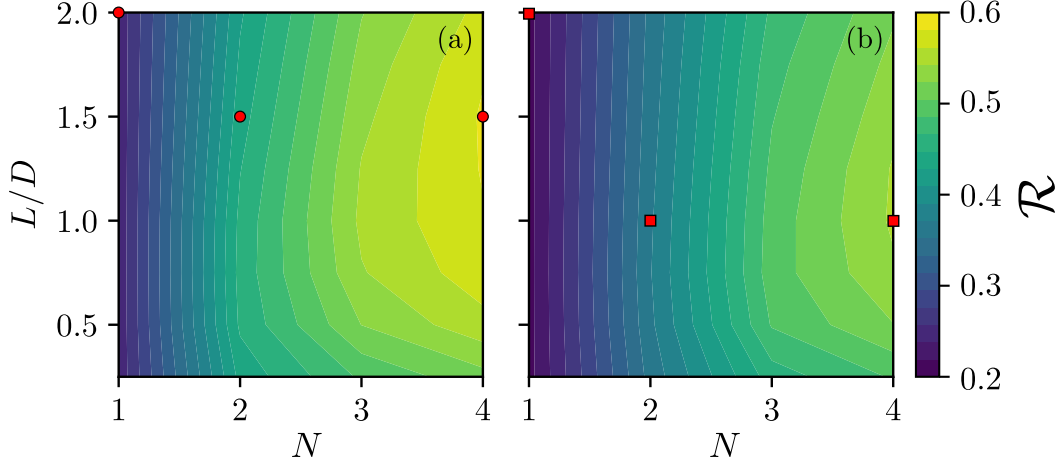


Figure 5: Summary of the energy reduction \mathcal{R} given by Eq. (31) with respect to the aspect ratio L/D and to the number of dishes in parallel N .

and $1 \leq N \leq 4$, at the two locations in the study. Fixed $D = 1$ m as a reference diameter of the TES, the sensitivity analysis in Fig. 5 illustrates that the maximum energy savings in Q_{add} occur for $N = 4$ dishes in parallel and for the aspect ratios $L/D = 1.5$ in Córdoba and $L/D = 1.0$ in Málaga.

Unlike Van Lew et al. [44], where the sizing of a molten salt tank (with similar charge/discharge operation modes) was calculated for steady state inlet conditions, the current approach offers a more accurate tool capable of handling time-dependent inlet temperatures. Figure 6 and Fig. 7 in Sect. 4.3 depict the time evolution of some magnitudes of interest for the selected points marked in Fig. 5 at the two distinct locations, one of them representing, of course, the most suitable TES size according to this approach.

4.3. Combined dish-TES operation

Figures 6 and 7 show the numerical results of the whole cycle operation, according to the models in Sect. 3. For the various combinations of L/D and N selected in Fig. 5, these graphs show the daily evolution of the outlet temperatures from the solar dish and from the TES, as well as the additional power and added energy, for the selected days of the year. Note that the charge/discharge and bypass modes of the TES unit are identified in Figs. 6 and 7, providing useful information for cycle analysis.

For the cases where only one dish has been considered, Figs. 6 and 7(a), (d), and (g), it can be shown that the solar input cannot overcome the reference temperature during that day on its own, indicating that neither charge nor discharge processes occur at any of the chosen locations, and the TES is always bypassed. As a result, the energy captured by the solar dish is the only input

received by the industrial process, which must be backed up by the added external power (see the power curve mirroring that of the solar dish outlet temperature T_{SD}). In the best cases (on 22nd June), this leads to an energy consumption of 434 and 451 kWh in Córdoba and Málaga, respectively, which represents about 30–33% energy savings with respect to cycle performance without any support. On December 22nd, the solar contribution is much scarce, and the energy savings decay to 3.8–2.6%.

Alternatively, if two solar dishes are used in parallel configuration, the dish outlet temperatures increase considerably, and some of the cases in Figs. 6 and 7(b), (e) and (h) enables the TES operation. For example, regarding the results on March 22nd in Córdoba [see Fig. 6(b)], it can be observed that there is a time window around noon where T_{SD} becomes higher than T_{ref} , and consequently, the TES charge is activated. Later, once T_{SD} decays below T_{ref} , the bypass mode is activated until discharge begins, when T_{SD} further decreases below the TES temperature in bypass mode (T_{TES}^{bp}). The energy savings in this case are $\simeq 45\%$, which is substantially greater than those obtained with $N = 1$. It is worth mentioning that the TES charge/discharge modes are not reached in Málaga [see Fig. 7(b)] resulting in energy savings of approximately a 30%, which are comparable to those obtained with $N = 1$ on June 22nd [see Figs. 6 and 7(d)]. On June 22nd, the con-

tribution of the dish raises the air temperature above T_{ref} during most of the solar hours both in Córdoba and Málaga [see Figs. 6 and 7(d)]. This fact leads to longer charge period from approximately 10 to 20 h, and minimizes the bypass actuation, which is of course beneficial (note that bypass mode generally implies $\dot{Q}_{add} > 0$). It can be observed that external power is added to the system during the first ten hours of the day, and a zero-energy window results for approximately the following 10 hours. The energy reduction under these circumstances is greater than 60%, i.e. twice the savings achieved in its counterpart with $N = 1$ in Figs. 6 and 7(d). In winter [Figs. 6 and 7(d)], the solar power captured by the dish is not enough to overcome the reference temperature, and back up power becomes necessary. The savings in this case are slightly higher than those in Figs. 6 and 7(g), but in any case they are below 8%.

Finally, when four dishes are connected in parallel, the temperature of the air exiting the solar dish is further increased with respect to the previous configurations, reaching considerably peak values of about 1400, 1700, and 700 °C in both locations. On March 22nd and on June 22nd, it can be seen in Figs. 6 and 7(c) and (f) that $T_{SD} > T_{ref}$ for practically all the solar hours, enabling the charge mode of the TES during that period, and the discharge from the sunset until the end of the day. The bypass mode is barely active (only for

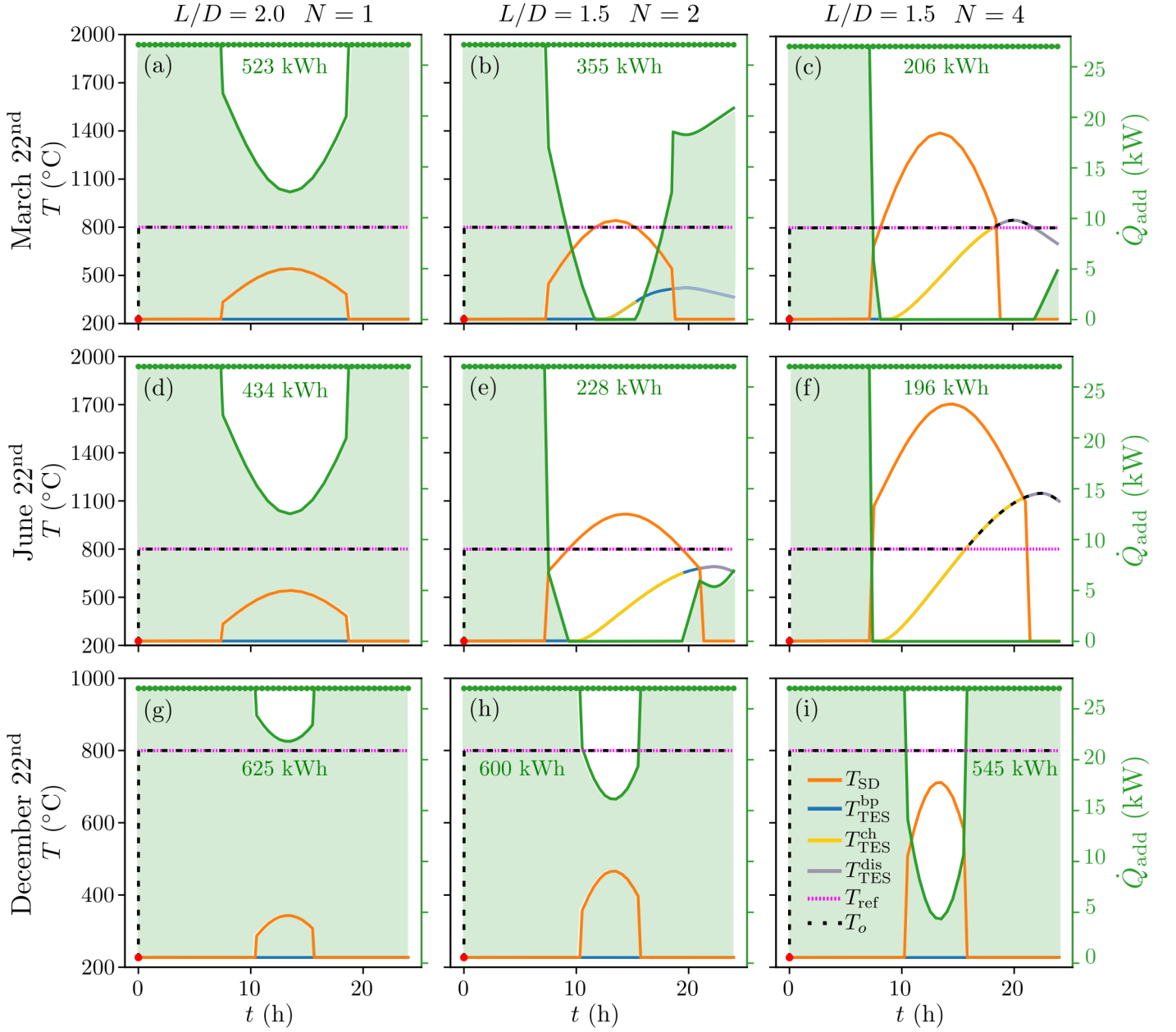


Figure 6: Transient evolution of the solar-dish outlet temperature T_{SD} (orange), and of the air temperatures in the TES in bypass mode T_{TES}^{bp} (blue), in charging mode T_{TES}^{ch} (yellow), and in discharge mode T_{TES}^{dis} (grey). The reference temperature T_{ref} and the produced temperature are depicted by dashed lines in pink and black, respectively. The right-hand side scale accounts for the additional heat power \dot{Q}_{add} to meet the industrial demand of 27 kW (bullets line in green). The shaded green area represents the back up energy consumed during the day given by Eq. (34). The total amount of energy is superimposed (in green). All these results refer to March 22nd, June 22nd and December 22nd in Córdoba, for the configurations indicated on the top.

a short period in Fig. 7(f)). This configuration only requires extra energy during the first third of the day and in the last 2–4 hours, depending on the location [see Fig. 6(c) vs. Fig. 7(c)]. The

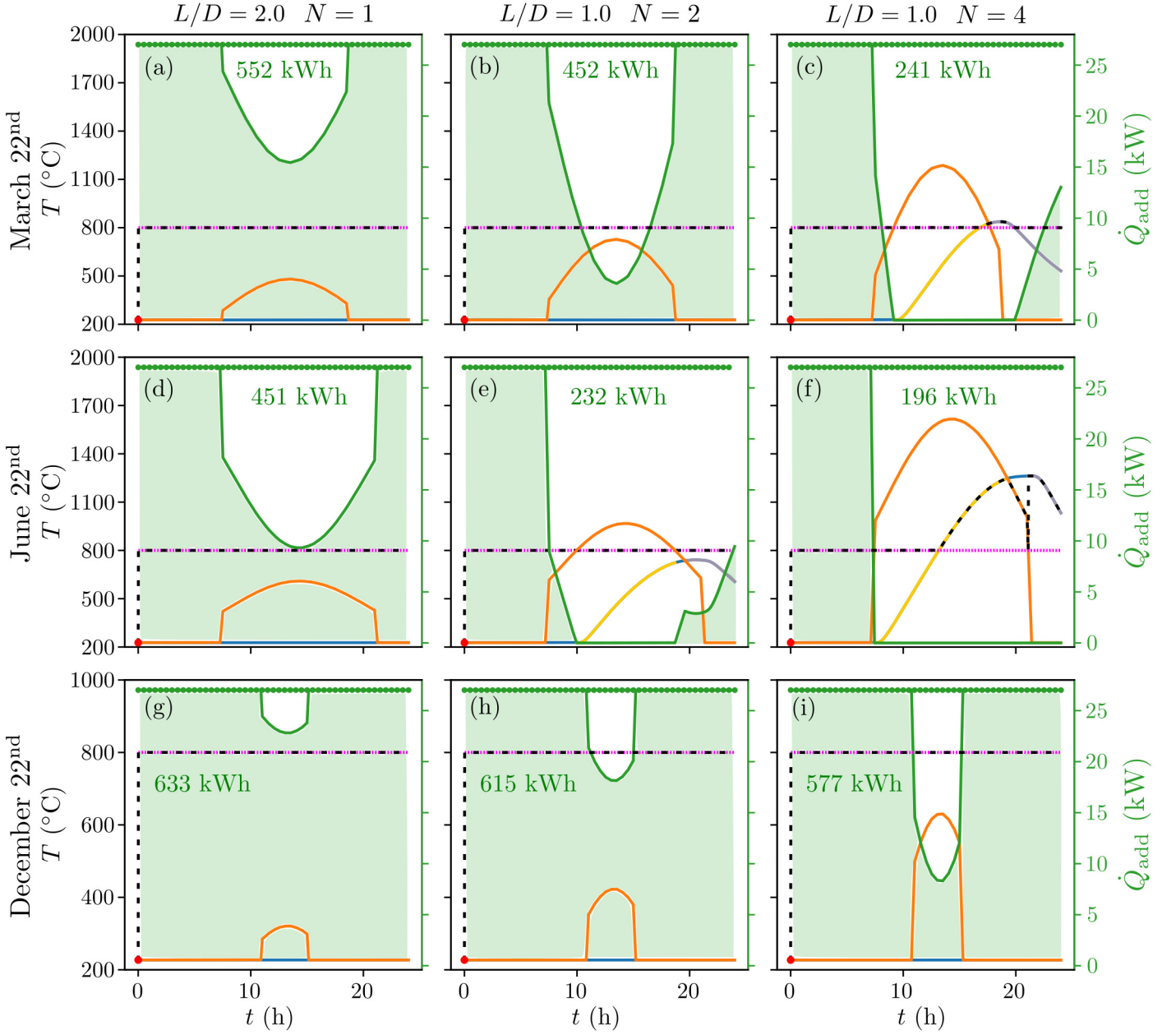


Figure 7: Same as in Fig. 6 but for Málaga.

respective energy reduction on March 22nd and on June 22nd rises up to a 63–68% and a 70%. The energy savings in winter are small, but somewhat larger than with the $N = 2$ configuration (16% in Córdoba and 11% in Málaga).

In summary, one can note that the larger the number of dishes in parallel configuration, the

higher the air temperature, and therefore the greater the energy amount that can be stored in the TES unit. Figure 5 illustrates that the TES size needs to be determined analyzing the energy requirements of the cycle. In this work, an energy-based decision-making algorithm has been implemented for simplicity, and the TES size has been

adopted accordingly. However, one can see that the energy contained in the thermal battery is not fully discharged at the end of the day, which would set the air temperature at a higher level for the next day, and in practice would indicate that the actual TES size might be smaller. Because the ultimate aim for the real implementation of this proof-of-concept is to estimate the ROI (return of inversion), a more accurate TES sizing approach will be proposed for future studies, conducting numerical simulations either during more days or analyzing the sensitivity of the initial temperature in the TES.

4.4. Economic savings and environmental impact

Besides the former results in terms of thermal energy and power, it is also convenient to quantify the economic aspects and the CO₂-equivalent emissions (the latter also involving economic benefits but not considered here) in operating conditions. The electric market will be considered here because historical data on the evolution of Spanish grid pricing are freely available from Red Eléctrica Española [45].

At first glance, one can observe in Fig. 8(a) or (b) that while the theoretical energy price on March 22nd is comparable to that on June 22nd, it was much lower on December 22nd, mainly due to the wind energy generation. From these rates, the accumulated theoretical prices resulted in about 240, 210 and 75 EUR at the end of the respective days. If one solar dish is introduced, the contribu-

tion is clearly observed during the central hours of the day, e.g. through a decreasing curve in (a) and (c), or through a smaller-slope period in (b) and (d). The maximum cost reduction per hour is reached on June 22nd and it is about four times with respect to the instantaneous energy price. However, at the end of the day, the total cost is comparable to that on March 22nd, i.e. around 160 EUR. The winter day is by far cheaper than the other two, but this is exclusively due to the fact that the electricity pricing on December 22nd was rather low compared to the other days of the study.

Some periods of free energy can be reported (see Fig. 8) when the cycle is implemented with four dishes in parallel. For example, the operating price in (a) and (c) drops to zero from 9 h until the end of the day on 22 Junend, and virtually the same on March 22nd. This can be observed as a plateau in the charts (b) and (d), where the accumulated price no longer increases. The total price at the end of the day is about 50 and 75 EUR under this scenario. By comparison, on December 22nd, the free energy condition is not met and the final price results in $\simeq 62$ EUR.

Alternatively, Fig. 9 compares (a) the additional energy and (b) its (electric) cost for the different CSP-TES configurations in Córdoba and Málaga, for each day of the study. It is evident that Q_{add} decreases monotonically with the number of dishes in parallel configuration, which is

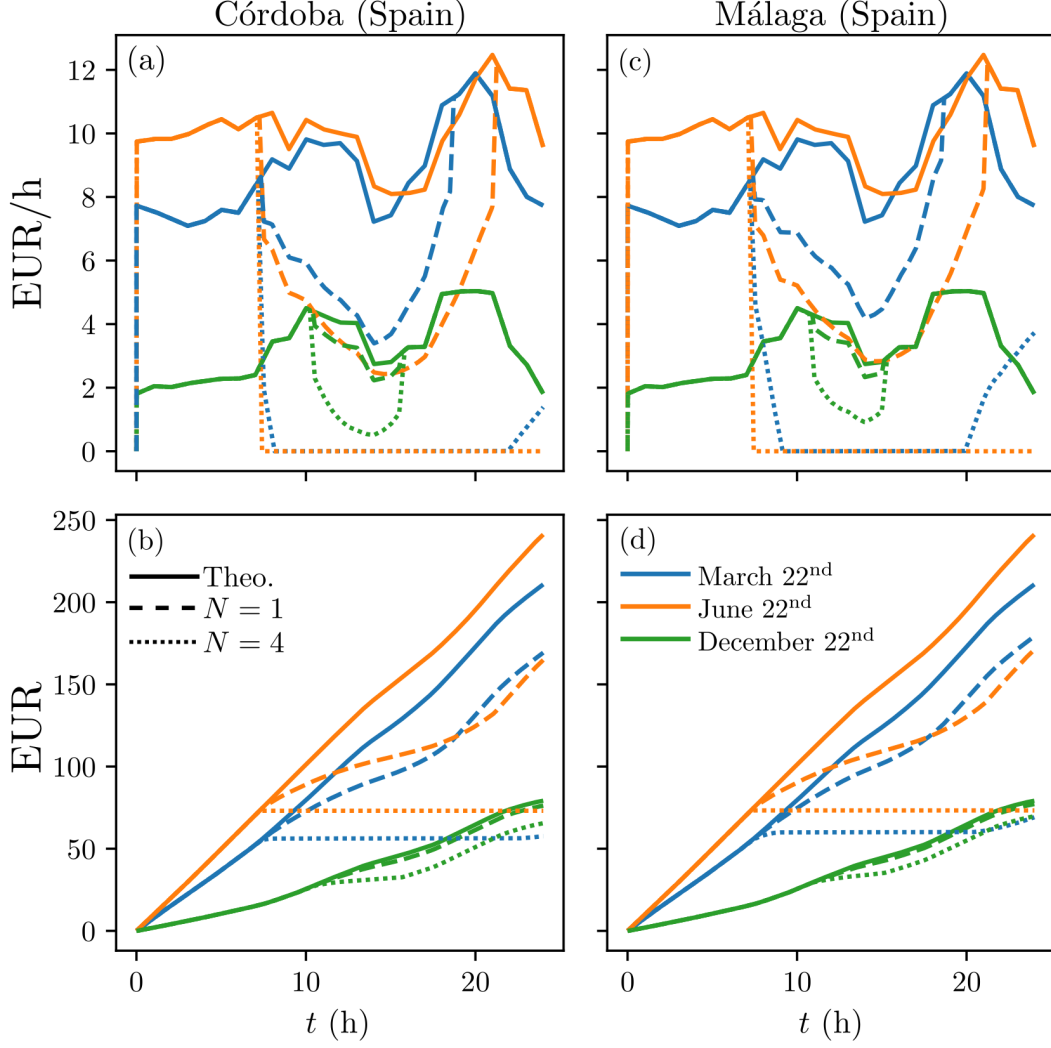


Figure 8: Transient evolution of the respective cost per hour and of the (accumulated) cost in Córdoba (a), (b) and in Málaga (c), (d), for the days in the study. Solid line: theoretical cost satisfying the industrial demand without dish or TES, dashed: cost with $N = 1$ solar dish and $L/D = 2$, dotted: cost with $N = 4$ dishes in parallel and $L/D = 1.5$ (for Córdoba) and $L/D = 1.0$ (for Málaga).

basically an illustrative summary of Fig. 6 and Fig. 7. Obviously, the days with a smaller input of Q_{add} are those receiving more solar radiation, i.e. March 22nd and June 22nd at both locations. Although it had been discussed that the environmental conditions of Córdoba and Málaga are quite similar, there is a noticeable difference of $\simeq 100$ kWh in Fig. 9(a) on March 22nd. How-

ever, in economic terms, it does not follow the same trend because the amount of renewable energy production (see Sect. 4.4 in terms of CO_2) on December 22nd reduced the prices of the electric market substantially, as it can be observed in Fig. 9(b). This situation leads to the case where $N = 4$, and Q_{add} is so small (due to the large received energy) that it surpasses (or compensates)

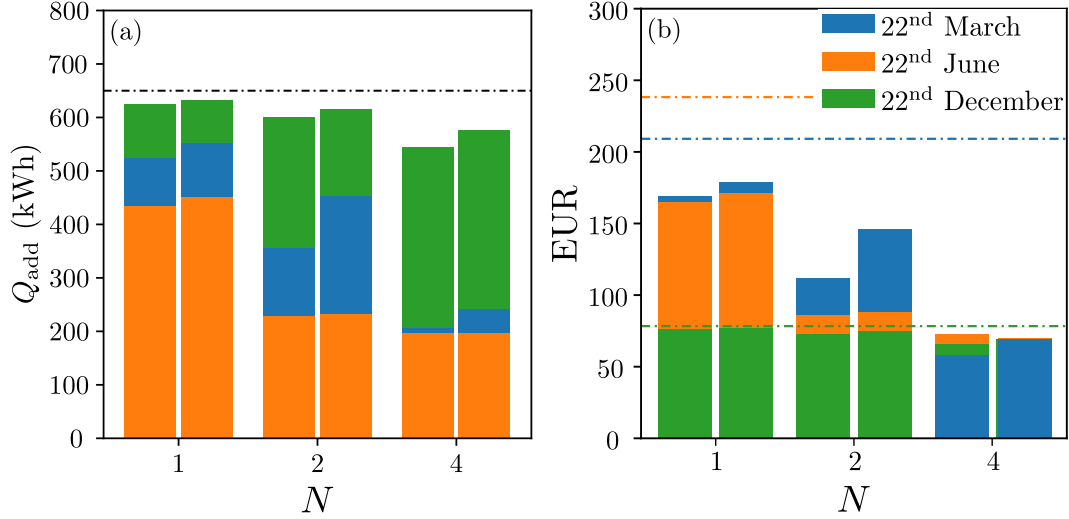


Figure 9: Comparison of the overall energy (a) and cost (b) of the cycle operation for the different configurations marked in Eq. (31), for each of the days in the study. Left columns of each pair indicate Córdoba, and right columns Málaga. Black dashed-dotted line is the required theoretical energy, and colored dashed-dotted lines indicates the accumulated cost per each of the days in the legend.

the excessively cheap price of energy on December 22nd. Particularly, the cost in Córdoba follows the Q_{add} trend in (a) (i.e. the larger the additional energy, the more expensive the system operation on that day). In Málaga, it barely reaches an equilibrium point, meaning that regardless of the day in analysis, the operation cost will remain the same.

In terms of CO₂ emissions, Sect. 4.4 summarizes the equivalent quantity in kilograms, comparing the result obtained under different configurations (N , L/D) for each of the days and locations in this study. As a reference, the total amount of emissions when operating only by consuming electrical energy from the Spanish grid (theoretical case) are 71, 105 and 39 CO₂ eq. kg on March 22nd, June 22nd and on December 22nd, respectively. A general look at Sect. 4.4

shows that the amount of CO₂ emissions is consistent with the price of energy because lower emissions mean more renewable generation and consequently a more competitive energy pricing. With $N = 1$, the percentage of reduction with respect to the theoretical case represents approximately 15%, 26%, and 2%, respectively. If two dishes are connected in parallel, the decarbonization of the industrial activity may reach 37%, 57%, and 5%. The highest CO₂ cut corresponds to the parallel configuration with $N = 4$ dishes, avoiding 63%, 63%, and 13% CO₂ emissions with respect to the baseline.

Finally, because the decision-making algorithm applied in this work is purely temperature-based, these new insights are exclusively informative, but as previously commented, it gives some guidelines to minimize important alternative aspects such

Table 2: CO₂-equivalent emissions at each location for each day of the study. For $N = 1$, $N = 2$ and $N = 4$, CO₂-eq. kg in Córdoba / CO₂-eq. kg in Málaga.

	March 22 nd	June 22 nd	December 22 nd
Theo.	71	105	39
$N = 1$	59 / 62	77 / 79	38 / 38
$N = 2$	41 / 52	45 / 45	37 / 37
$N = 4$	24 / 28	39 / 39	34 / 35

as the ROI of the proposed system or the CO₂ removal (CDR).

As an example, consider a final industrial activity consuming natural gas (NG) at a fixed combustion rate ensuring 650 kWh per operational day. Following e.g. Steen et al. [46], the CO₂ emission factor from NG-fired power generation is estimated to be in the range 56–78 CO₂-eq. kg/MJ, resulting in 131–182.5 CO₂-eq. kg/day in all. These values are in general higher than those from the theoretical case reported in Sect. 4.4, in which the system is fully powered by the Spanish electric grid. The highest CDR would be achieved on December 22nd because of intense renewable production. In contrast, the 105 CO₂-eq. kg emitted on June 22nd are only $\simeq 25\%$ (26 kg) smaller with respect to the lower limit of the range estimated from NG (131 kg/day). This explains that despite the high production of PV energy on that day (of course during sunny hours), a considerable amount of fossil fuels was necessary to compensate for the decrease in wind and hydraulic energy generation (the latter induced by drought periods)[45].

5. Conclusions

The unsteady simulation of a combined CSP-TES proof of concept delivering constant high-temperature heat has been analyzed numerically in this work. It aims to decarbonize a given industrial activity (e.g. cement, glass, chemicals, etc.) in two reference locations of Andalusia (southern Spain): Córdoba and Málaga, on the days March 22nd, June 22nd and December 22nd (i.e. two solstices and one equinox). To this end, the influence of a single solar dish or multiple dishes in parallel configuration together with a TES unit size have been evaluated through a sensitivity analysis considering two main dimensionless parameters, namely the number of dishes N and the TES aspect ratio L/D . The results have shown that the configuration $L/D = 1$ (in Córdoba) or $L/D = 1.5$ (in Málaga) is that providing the maximum reduction of the back up energy required to ensure the demanding heat of 27 kW at 800 °C ($\simeq 650$ kWh).

Considering that the TES unit is uniformly charged at the waste/return temperature at start,

a simple decision-making algorithm has been implemented to analyze the unsteady operation of the device, dealing with charge, discharge or bypass strategies. In general, it has been shown that the TES unit plays a role in the system when the solar-dish outlet temperature exceeds that of the reference, e.g. on March 22nd and on June 22nd with $L/D = 1.5$ and $N \geq 2$, in Córdoba. The results are very similar to those in Málaga, except for the case on March 22nd with $N = 2$ and $L/D = 1.0$, where no TES operation takes place. Although the applied strategy seems reasonable, there are some cases in which the TES unit is not fully discharged at the end of the day, resulting in a waste of energy. This fact motivates further studies to consider several consecutive days for the TES sizing. Alternatively, since the waste temperature and that of the demand could change depending on the industrial activity, a sensitivity analysis ranging along different values could result of interest to characterize the performance of the proposed system.

In economic terms, the impact of the CSP-TES combined solution has been analyzed assuming that the additional energy to meet the heat demand is accomplished by means of electric energy from the Spanish grid. This study has shown that although the electric price on December 22nd was extremely low due to a high renewable energy production, the use of the CSP-TES system has resulted in savings of up to a 33% with one dish, a

66% with two, and a 69% with four dishes, compared to the case operating with only electrical energy.

Furthermore, the CO₂ footprint has also been evaluated by means of the emissions derived from the instantaneous generation structure of electricity in the Spanish grid. Simulations have shown that the CO₂ removal is considerable, emitting up to 28, 60, and 66 fewer equivalent kg with respect to the baseline case. For illustration, an simple application example has been included to show the important CO₂ removal of the proposed proof of concept with respect to the reference industrial activity exclusively operating with natural gas.

In summary, the evaluation of the proposed CSP-TES system has revealed suitability for practical implementation, considering both energetic, economic and environmental aspects. It has been shown that the role of the TES unit with an appropriate control logic is essential for the system operation. Moving forward, further research could focus on refining the TES sizing methodology and exploring adaptive control strategies to optimize system performance under varying operational conditions.

Appendix A. Validation

Appendix A.1. Solar dish

The solar dish model in Eqs. (1) to (9) has been validated against the experimental measurements of Zhu et al. [8] in Table A.3. In terms of thermal

efficiency Eq. (19), the solar dish model implemented in this study provided $\eta = 81.27\%$, which is quite in agreement with the experimental measurements of Zhu et al. [8] (81.5%), at the same mass flow rate $\dot{m} = 0.043$ kg/s. Efficiency was obtained from the heat losses depicted in Fig. A.10, computed by means of Eqs. (12) to (17).

Table A.3: Validation of the numerical results provided by the solar dish model in Eqs. (1) to (8).

T ($^{\circ}\text{C}$)	Num.	Ref.[8]
T_i	56.00	—
T_1	77.08	77.0
T_2	99.17	90.9
T_3	107.51	97.0
T_4	478.44	495.8
T_f	585.95	300.5
T_w	389.68	257.6
T_{gi}	404.34	233.1
T_{go}	354.11	
T_o	453.16	~ 450

Note that the results depicted in Fig. A.10 may differ slightly from those of Zhu et al. [8] due to the different thermal coefficients adopted in each work. However, the trend in heat power losses is similar and the global efficiency is below 0.3 % with respect to the experiments.

Appendix A.2. Thermal Energy Storage (TES)

As in previous studies [12, 14, 15, 37, 47], the validation of Eqs. (20) to (24) has been carried

out against the experimental results of the thermocline tank pilot at Sandia National Laboratories [41], and with those of [22, 48], resulting in a good agreement for both cases. The choice of $\Delta t = 3.6$ s and $\Delta x = 1.2$ cm [14, 37] was in reasonable agreement with the reference, as shown in Fig. A.11. The CFL condition ($u\Delta t/\Delta x$) resulting from this configuration is maintained below 1, which ensures the stability of the simulations [38].

The thermophysical properties of the molten salts and quartzite [14, 44], and air [49] and rock [48] adopted in the simulations are shown in Table A.4.

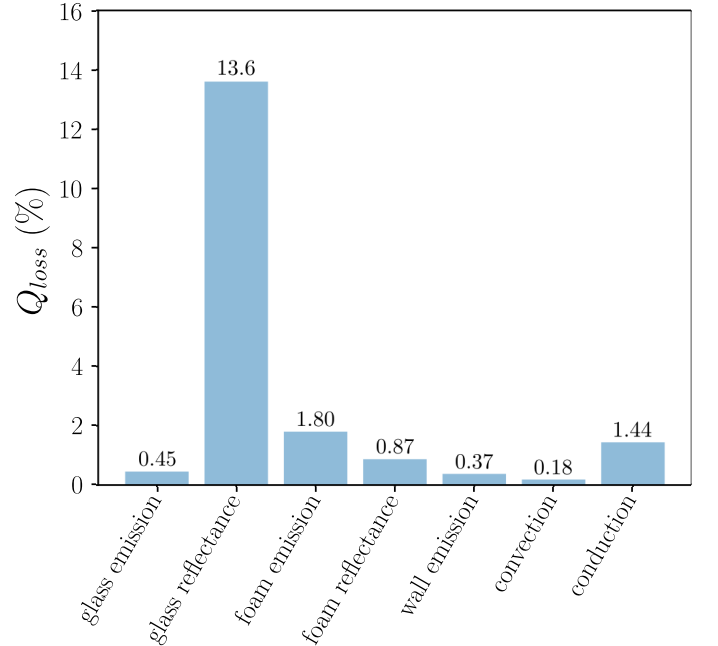


Figure A.10: Thermal losses in the validation case [8] computed with the current model of the solar dish.

Table A.4: Thermophysical properties of the HTF and of the packed bed material (temperatures in K where needed).

Solar salt	ρ_f	kg m^{-3}	$2090 - 0.636 T$
	C_{pf}	$\text{J kg}^{-1} \text{K}^{-1}$	$1443 + 0.172 T$
	k_f	$\text{W m}^{-1} \text{K}^{-1}$	$0.443 + 1.9 \times 10^{-4} T$
	μ_f	Pa s	$(22.174 - 0.12 T + 2.281 \times 10^{-4} T^2 - 1.471 \times 10^{-7} T^3)/1000$
Quartzite rocks	ρ_s	kg m^{-3}	2640
	C_{ps}	$\text{J kg}^{-1} \text{K}^{-1}$	1050
	k_s	$\text{W m}^{-1} \text{K}^{-1}$	2.5
Compressed air (5 bar)	ρ_a	kg m^{-3}	15.4
	C_{pa}	$\text{J kg}^{-1} \text{K}^{-1}$	1032
	k_a	$\text{W m}^{-1} \text{K}^{-1}$	0.037
	μ_a	Pa s	2.53×10^{-5}
Rock	ρ_r	kg m^{-3}	2560
	C_{pr}	$\text{J kg}^{-1} \text{K}^{-1}$	960
	k_r	$\text{W m}^{-1} \text{K}^{-1}$	0.48

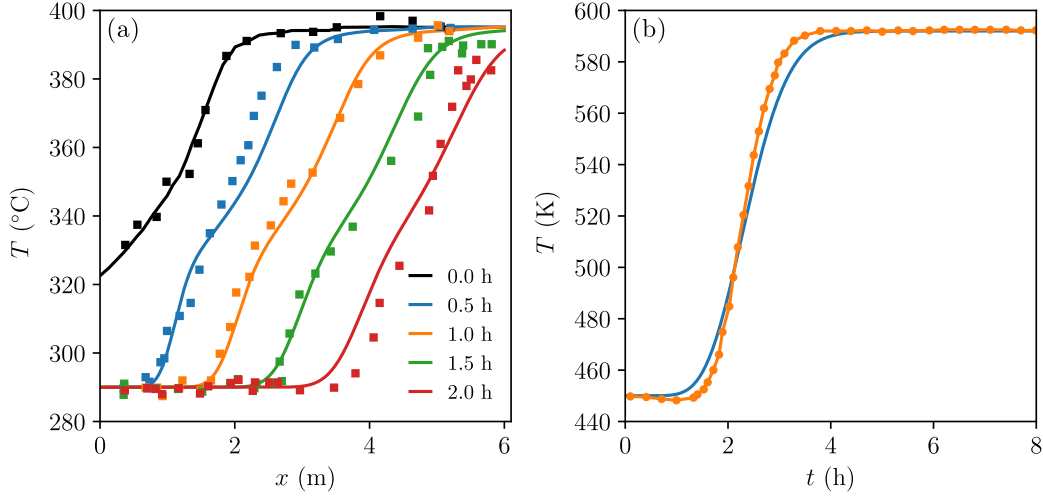


Figure A.11: Comparison of the numerical results (solid lines) with the experimental data from Sandia Laboratory pilot for molten salts [41] (a), and with the results of [22, 48] (b) for air flowing through a rocks packed-bed tank. Thermophysical properties are given in Table A.4.

Appendix A.3. Thermal model of the glass window

The high concentration ratio of solar radiation entering the receiver along with the volumetric absorption effects taking place into the thickness of the glass window L_g , makes it interesting to model this phenomenon. It implies the use of two different temperature values on both sides or borders of the glass window: $T_{g,i}$ and $T_{g,o}$ and the volumetric source term, which is defined based on the assumption that all visible radiation \dot{q}_v absorbed by the glass windows is homogeneously distributed throughout its volume. Only the direct concentrated solar beam I_b together with that reflected by the foam has been approximated as follows.

$$\dot{q}_v = \frac{\alpha_g I_b + \tau_g I_b F_{fg} \rho_f}{L_g}. \quad (\text{A.1})$$

This source term acts as an internal volumetric generation term within the glass domain to solve the 1D diffusion equation, based on a local coordinate system \hat{x} and constant thermal conductivity $k_g = 1.4 \text{ W m}^{-1} \text{ K}^{-1}$ of the medium,

$$T(\hat{x}) = -\frac{\dot{q}_v \hat{x}^2}{2k} + \left[\frac{T_{gi} - T_{go}}{L_g} + \frac{\dot{q}_v L_g}{2k_g} \right] \hat{x} + T_{go}. \quad (\text{A.2})$$

From the temperature profile $T(\hat{x})$ across the glass window and Fourier's Law, heat transferred at each border can be defined,

$$\dot{q}_{g,o} = k_g \frac{T_{g,o} - T_{g,i}}{L_g} - \frac{\dot{q}_v L_g}{2}, \quad (\text{A.3})$$

$$\dot{q}_{g,i} = k_g \frac{T_{g,o} - T_{g,i}}{L_g} + \frac{\dot{q}_v L_g}{2} = \dot{q}_v L_g + \dot{q}_{g,o}. \quad (\text{A.4})$$

References

- [1] European Commission, Communication from the Commission to the European Parliament, the European Council, the Council, the European Economic and Social Committee and

- the Committee of the Regions - REPowerEU Plan - COM(2022) 230 final, 2022. URL: <https://eur-lex.europa.eu/legal-content/EN/TXT/?uri=COM%3A2022%3A230%3AFIN>.
- [2] Directorate-General for Energy (European Commission), EU energy in figures - STATISTICAL POCKETBOOK, 2023. URL: <https://op.europa.eu/en/publication-detail/-/publication/bb9f16ee-642f-11ee-9220-01aa75ed71a1>.
- [3] S. Madeddu, F. Ueckerdt, M. Pehl, J. Peterseim, M. Lord, K. A. Kumar, C. Krüger, G. Luderer, The co2 reduction potential for the european industry via direct electrification of heat supply (power-to-heat), *Environmental Research Letters* 15 (2020) 124004.
- [4] X. Ma, Y. Du, B. Lei, Y. Wu, Energy, exergy, economic, and environmental analysis of a high-temperature heat pump steam system, *International Journal of Refrigeration* (2024).
- [5] Red Eléctrica, Informe del Sistema Eléctrico - Informe resumen de energías renovables 2022, 2023. URL: https://www.sistemaelectrico-ree.es/sites/default/files/2023-03/Informe_Renovables_2022.pdf.
- [6] I. Heras-Saizarbitoria, E. Cilleruelo, I. Zamanillo, Public acceptance of renewables and the media: an analysis of the spanish pv solar experience, *Renewable and Sustainable Energy Reviews* 15 (2011) 4685–4696.
- [7] J. Coventry, C. Andraka, Dish systems for csp, *Solar Energy* 152 (2017) 140–170.
- [8] J. Zhu, K. Wang, Z. Jiang, B. Zhua, H. Wu, Modeling of heat transfer for energy efficiency prediction of solar receivers, *Energy* 190 (2020) 116372.
- [9] J. García Ferrero, R. Merchán, M. Santos, A. Medina, A. C. Hernández, P. Canhoto, A. Giostri, Modeling a solar pressurized volumetric receiver integrated in a parabolic dish: Off-design heat transfers, temperatures, and efficiencies, *Energy Conversion and Management* 293 (2023) 117436.
- [10] International Renewable Energy Agency, Innovation Outlook: Thermal Energy Storage, 2020. URL: https://www.irena.org/-/media/Files/IRENA/Agency/Publication/2020/Nov/IRENA_Innovation_Outlook_TES_2020.pdf?rev=6950b7b9792344b5ab28d58e18209926.
- [11] S. Pascual, P. Lisbona, L. M. Romeo, Thermal energy storage in concentrating solar power plants: A review of european and north american r&d projects, *Energies* 15 (2022) 8570.
- [12] A. Abánades, J. Rodríguez-Martín, J. Roncal, A. Caraballo, F. Galindo, Proposal of a thermocline molten salt storage tank for district heating and cooling, *Applied Thermal Engineering* 218 (2023) 119309.
- [13] K. E. Elfeky, A. G. Mohammed, N. Ahmed, Q. Wang, Thermo-mechanical investigation of the multi-layer thermocline tank for parabolic trough power plants, *Energy* 268 (2023) 126749.
- [14] S. M. Flueckiger, B. D. Iverson, S. V. Garimella, J. E. Pacheco, System-level simulation of a solar power tower plant with thermocline thermal energy storage, *Applied Energy* 113 (2014) 86–96.
- [15] J.-F. Hoffmann, T. Fasquelle, V. Goetz, X. Py, A thermocline thermal energy storage system with filler materials for concentrated solar power plants: Experimental data and numerical model sensitivity to different experimental tank scales, *Applied Thermal Engineering* 100 (2016) 753–761.
- [16] F. Herbinger, M. Bhouri, D. Groulx, Investigation of heat transfer inside a pcm-air heat exchanger: a numerical parametric study, *Heat and Mass Transfer* 54 (2018) 2433–2442.
- [17] Y. Dutil, D. R. Rousse, N. B. Salah, S. Lassue, L. Zalewski, A review on phase-change materials: Mathematical modeling and simulations, *Renewable and sustainable Energy reviews* 15 (2011) 112–130.
- [18] M. A. Izquierdo-Barrientos, C. Sobrino, J. A.

- Almendros-Ibáñez, Thermal energy storage in a fluidized bed of pcm, *Chemical Engineering Journal* 230 (2013) 573–583.
- [19] A. Tiddens, M. Röger, H. Stadler, B. Hoffschmidt, Air return ratio measurements at the solar tower jülich using a tracer gas method, *Solar Energy* 146 (2017) 351–358.
- [20] E. E. John, W. M. Hale, R. P. Selvam, Development of a high-performance concrete to store thermal energy for concentrating solar power plants, volume 54686, 2011.
- [21] E. Villarroel, C. Fernandez-Pello, J. Lenartz, K. Parysek, High efficiency thermal storage system for solar plants (HELSOLAR). Final report, Technical Report, SENER Engineering and Systems, Inc., San Francisco, CA (United States), 2013.
- [22] M. Hänchen, S. Brückner, A. Steinfeld, High-temperature thermal storage using a packed bed of rocks–heat transfer analysis and experimental validation, *Applied Thermal Engineering* 31 (2011) 1798–1806.
- [23] R. Mei, Carbon Dioxide Shuttling Thermochemical Storage Using Strontium Carbonate, Technical Report, Univ. of Florida, Gainesville, FL (United States), 2015.
- [24] A. Energy, Antora, 2020. URL: <https://antoraenergy.com/>.
- [25] MIT Technology Review, The hottest new climate technology is bricks, 2023. URL: <https://technologyreview.com/2023/04/10/1071208/the-hottest-new-climate-technology-is-bricks/>.
- [26] M. Papapetrou, G. Kosmadakis, A. Cipollina, U. La Commare, G. Micale, Industrial waste heat: Estimation of the technically available resource in the eu per industrial sector, temperature level and country, *Applied Thermal Engineering* 138 (2018) 207–216.
- [27] A. Inayat, Current progress of process integration for waste heat recovery in steel and iron industries, *Fuel* 338 (2023) 127237.
- [28] International Renewable Energy Agency, Innovation Landscape for smart electrification: Decarbonising end-use sectors with renewable power, 2023. URL: https://mc-cd8320d4-36a1-40ac-83cc-3389-cdn-endpoint.azureedge.net/-/media/Files/IRENA/Agency/Publication/2023/Jun/IRENA_Innovation_Landscape_for_smart_electrification_2023.pdf?rev=b92a90a778df450ea79ee8527ac1e334.
- [29] A. Sanchez Sanchez de Puerta, J. L. Aranda-Hidalgo, A. Martín-Alcántara, Ciclo para suministro de calor renovable y estable con hibridación de almacenamiento térmico con diferentes inercias para procesos industriales de alta temperatura, Patent application number P202330972, Nov. 2023.
- [30] L. Migliari, S. Arena, P. Puddu, D. Cocco, Thermo-fluid dynamic analysis of a csp solar field line during transient operation, *Energy Procedia* 101 (2016) 1167–1174.
- [31] A. Cengel, Heat transfer, New York: McGraw-Hill, 2003.
- [32] A. Žukauskas, Heat transfer from tubes in crossflow, in: *Advances in heat transfer*, volume 8, Elsevier, 1972, pp. 93–160.
- [33] C. Zhao, T. Kim, T. Lu, H. Hodson, Thermal transport in high porosity cellular metal foams, *Journal of Thermophysics and Heat Transfer* 18 (2004) 309–317.
- [34] J. J. Moré, B. S. Garbow, K. E. Hillstrom, User guide for MINPACK-1, Technical Report, CM-P00068642, 1980.
- [35] P. Virtanen, R. Gommers, T. E. Oliphant, M. Haberland, T. Reddy, D. Cournapeau, E. Burovski, P. Peterson, W. Weckesser, J. Bright, S. J. van der Walt, M. Brett, J. Wilson, K. J. Millman, N. Mayorov, A. R. J. Nelson, E. Jones, R. Kern, E. Larson, C. J. Carey, Í. Polat, Y. Feng, E. W. Moore, J. VanderPlas,

- D. Laxalde, J. Perktold, R. Cimrman, I. Henriksen, E. A. Quintero, C. R. Harris, A. M. Archibald, A. H. Ribeiro, F. Pedregosa, P. van Mulbregt, SciPy 1.0 Contributors, SciPy 1.0: Fundamental Algorithms for Scientific Computing in Python, *Nature Methods* 17 (2020) 261–272. doi:10.1038/s41592-019-0686-2.
- [36] T. E. Schumann, Heat transfer: a liquid flowing through a porous prism, *Journal of the Franklin Institute* 208 (1929) 405–416.
- [37] K. Niedermeier, L. Marocco, J. Flesch, G. Mohan, J. Coventry, T. Wetzel, Performance of molten sodium vs. molten salts in a packed bed thermal energy storage, *Applied Thermal Engineering* 141 (2018) 368–377.
- [38] J. H. Ferziger, M. Perić, R. L. Street, *Computational methods for fluid dynamics*, springer, 2019.
- [39] C. R. Harris, K. J. Millman, S. J. van der Walt, R. Gommers, P. Virtanen, D. Cournapeau, E. Wieser, J. Taylor, S. Berg, N. J. Smith, R. Kern, M. Picus, S. Hoyer, M. H. van Kerkwijk, M. Brett, A. Haldane, J. F. del Río, M. Wiebe, P. Peterson, P. Gérard-Marchant, K. Sheppard, T. Reddy, W. Weckesser, H. Abbasi, C. Gohlke, T. E. Oliphant, Array programming with NumPy, *Nature* 585 (2020) 357–362. URL: <https://doi.org/10.1038/s41586-020-2649-2>. doi:10.1038/s41586-020-2649-2.
- [40] A. Butland, R. Maddison, The specific heat of graphite: An evaluation of measurements, *Journal of Nuclear Materials* 49 (1973) 45–56.
- [41] J. E. Pacheco, S. K. Showalter, W. J. Kolb, Development of a molten-salt thermocline thermal storage system for parabolic trough plants, *J. Sol. Energy Eng.* 124 (2002) 153–159.
- [42] P. W. Bridgman, *Dimensional analysis*, Yale university press, 1922.
- [43] A. Martín-Alcántara, J. L. Aranda-Hidalgo, A. Jiménez-Solano, A. J. Sarsa-Rubio, Analysis and design of an inverted oscillating water column for energy storage under choked flow conditions, *Energy* 285 (2023) 129356.
- [44] J. T. Van Lew, P. Li, C. L. Chan, W. Karaki, J. Stephens, Analysis of heat storage and delivery of a thermocline tank having solid filler material, *Journal of Solar Energy Engineering* 133 (2011) 021003, 1–10.
- [45] Red Eléctrica Española, REE, 2024. URL: <https://demanda.ree.es>.
- [46] M. Steen, et al., Greenhouse gas emissions from fossil fuel fired power generation systems, Institute for Advanced Materials, Joint Research Centre, European Commission (2001).
- [47] A. Modi, C. D. Perez-Segarra, Thermocline thermal storage systems for concentrated solar power plants: One-dimensional numerical model and comparative analysis, *Solar Energy* 100 (2014) 84–93.
- [48] H. Peng, R. Li, X. Ling, H. Dong, Modeling on heat storage performance of compressed air in a packed bed system, *Applied energy* 160 (2015) 1–9.
- [49] I. H. Bell, J. Wronski, S. Quoilin, V. Lemort, Pure and pseudo-pure fluid thermophysical property evaluation and the open-source thermophysical property library coolprop, *Industrial & Engineering Chemistry Research* 53 (2014) 2498–2508. doi:10.1021/ie4033999.